Longitudinal and spanwise vortical structures in a turbulent near wake

H. J. Zhang, Y. Zhou, and R. A. Antonia

Citation: Phys. Fluids **12**, 2954 (2000); doi: 10.1063/1.1309532
View online: http://dx.doi.org/10.1063/1.1309532
View Table of Contents: http://pof.aip.org/resource/1/PHFLE6/v12/i11
Published by the American Institute of Physics.

Longitudinal and spanwise vortical structures in a turbulent near wake

H. J. Zhang and Y. Zhou
Department of Mechanical Engineering, The Hong Kong Polytechnic University, Hung Hom, Kowloon, Hong Kong, China

R. A. Antonia
Department of Mechanical Engineering, University of Newcastle, N.S.W., 2308, Australia

(Received 13 January 2000; accepted 24 July 2000)

Approximations to the three vorticity components have been simultaneously obtained using a combination of four *X* wires in the near wake of a circular cylinder with the view of investigating the most likely interrelationship between quasilongitudinal rib-like structures and spanwise vortical structures. The conditional spanwise vorticity variance, based on detections of spanwise structures, shows a strong peak near the detections. This peak suggests a longitudinal extent of 1.0–1.3 cylinder diameters for the spanwise structures. The conditional streamwise vorticity variance has maxima near the saddle points on both sides of the detections, while the conditional lateral vorticity variance is maximum only downstream of the detections. The observations are interpreted in the context of rib-like structures wrapping around consecutive spanwise structures of opposite sign, a scenario which conforms with previous observations based on flow visualizations and direct numerical simulations. The probability density function of vorticity vectors in the plane of mean shear further suggests that the most likely inclination of the rib-like structures to the streamwise direction is about 50°. About 40% of the variances of streamwise and lateral vorticity components is associated with the spanwise vortical structures, apparently resulting from the three dimensionality of these structures; the ''remainder'' is largely attributed to the rib-like structures. Spanwise structures account for about 60%–80% of the spanwise vorticity variance. © *2000 American Institute of Physics.* [S1070-6631(00)51411-1]

I. INTRODUCTION

Previous research on the turbulent near wake has revealed two main types of vortical structures, which contribute to the three dimensionality of this flow: a quasi-two-dimensional spanwise structure with predominantly spanwise vorticity and quasilongitudinal structures in the (x, y) plane (see Fig. 1 for the definition of the coordinate system) with x and y components of vorticity.[1,2] The latter structures are rib-like and either wrap around or connect consecutive spanwise structures.[3,4] The presence of rib-like structures (for convenience, the term ''ribs'' will be used henceforth) has been confirmed by flow visualizations in near wakes at low Reynolds numbers.[5–8] Using hot-wire data, Zhou and Antonia[9] provided evidence of the existence of ribs at higher Reynolds numbers. However, several aspects, such as the dynamical role of ribs, the spatial relationship between ribs and spanwise structures, as well as the contributions these structures make to the vorticity variance require further investigation.

Vorticity is an important characteristic of turbulence. The vortical structures are characterized by large-scale vorticity concentrations. Hussain and Hayakawa[1] advocated that vorticity is the least ambiguous quantity to use for identifying organized structures. Insight into the interrelationship between the two types of structures may be gained by investigating the vorticity field. An accurate measurement of vorticity requires a reliable estimation of velocity gradients. This has proven generally difficult, as reflected by the scarcity of published data, especially for all three-components of the vorticity vector; adequately resolved single point data have been possible only under specially designed experimental conditions.[10] Using a combination of four *X* wires, Bisset *et al.*[11] measured all three components of vorticity in the far wake of a slightly heated cylinder. One drawback of this approach is that since vorticity is indirectly computed from velocity signals using the central difference approximation, the spacing between *X* wires may degrade the spatial resolution of vorticity. This degradation worsens at higher Reynolds numbers since the Kolmogorov length scale decreases when Re_d increases.[12] Balint *et al.*[13,14] used a nine-sensor hot-wire probe to measure the three components of vorticity in both the mixing layer and the boundary layer. Similar attempts have been made by Tsinober *et al.*[15] and Lemonis[16] in grid and boundary layer flows. Marasli *et al.*[17] measured the three components of vorticity in a circular cylinder wake ($x/d = 30$, where x is the streamwise distance downstream of the cylinder and d is the diameter of cylinder) with a twelve sensor hot-wire probe. In the present investigation, an approach similar to that of Bisset *et al.*[11] is used for approximating the three vorticity components. Although the spatial resolution is poor, the approximation is relatively easy to implement and should be adequate for describing the relatively large-scale vorticity field. Since longitudinal structures are expected to have intermediate scales, not drastically different from those of the spanwise structures,[4] the approach is likely to provide useful qualitative information on both

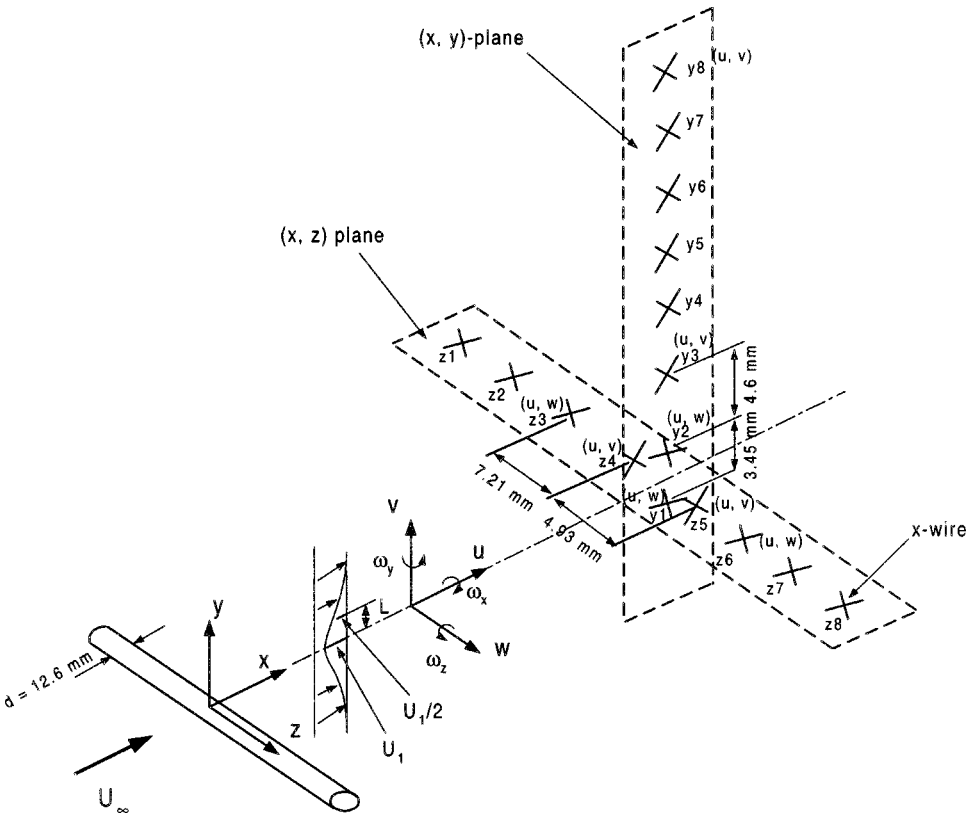

FIG. 1. Experimental arrangement.

streamwise structures and spanwise structures. Results are presented for (rms) values and spectra of the three vorticity components, the inclination of the vorticity vector, the conditional vorticity variance based on detections of spanwise structures, and contributions from different types of vortical structures and of the ''remainder'' to the vorticity variance.

II. EXPERIMENTAL ARRANGEMENT

Experiments were carried out in an open return low turbulence wind tunnel with a 2.4-m-long working section ($0.35\,\mathrm{m}\times0.35\,\mathrm{m}$). The bottom wall was tilted to achieve a zero streamwise pressure gradient. A circular cylinder ($d=12.7\,\mathrm{mm}$) was installed in the midplane and spanned the full width of the working section, 0.20 m from the exit plane of the contraction. This resulted in a blockage of about 3.6% and an aspect ratio of 27.6. Although the aspect ratio is relatively low, the deployment of the probes in the (x,z) plane allowed the spanwise uniformity of the flow to be checked. The mean velocity and turbulence intensities were reasonably uniform across most of the wake at a value of Re ($\equiv U_\infty d/\nu$, where U_∞ is the free stream velocity and ν is the kinematic viscosity) of 5600, which is the Reynolds number used for this investigation. No attempt was made to manipulate the end boundary conditions, although it has now been shown (Williamson;[18] Prasad and Williamson[19]) that it is possible to control oblique and parallel shedding at Reynolds number as large as 5000. The measurements were made at $x/d=20$. The mean velocity half-width was 12.6 mm. The free stream longitudinal turbulence intensity was about 0.05%.

Two orthogonal arrays, each comprising eight *X* wires (Fig. 1), were used. Four *X* wires, i.e., *X* wires y1, y2, z4, and z5, were arranged in similar fashion to Bisset *et al.*[11] They essentially formed a ''vorticity probe,'' which simultaneously yields (large-scale only) approximations to three components of vorticity. *X*-wires y1 and y2 were parallel to the (x, z) plane (see Fig. 1). The spacing between y1 and y2 was 3.45 mm. *X*-wires z4 and z5, with a spacing of 4.9 mm, were parallel to the (x, y) plane, i.e., the plane of mean shear. Six other *X* wires were aligned in the (x, y) plane, and six in the (x, z) plane. The six *X* wires, i.e., z1–z3 and z6–z8, in the (x, z) plane are not used in the analysis presented in this paper. The sixteen *X* wires allow velocity data to be obtained simultaneously. The nominal spacing between *X* wires in both planes was about 5 mm. The Kolmogorov length scale η was about 0.16 mm. All wires were mounted on a frame that was traversed in the *y* direction. The physical blockage caused by these arrays, cables, and supports was estimated to be about 3%. Several types of measurements indicated that the interference to the flow due to the two arrays was negligible.[9]

Wollaston (Pt-10% Rh) wires, 5 μm in diameter and with an active length of about 1 mm, were operated with constant temperature circuits. Signals from the circuits were offset, amplified, and then digitized using two 16 channel (12 bit) analog-to-digital boards and two personal computers at a sampling frequency $f_{\mathrm{sampling}}=3.5\,\mathrm{kHz}$ per channel. The acquisition of the data by the two computers was synchronized using a common external trigger pulse. The wires were calibrated for velocity and yaw, and continuously checked for drift. Using velocity and yaw calibrations, signals propor-

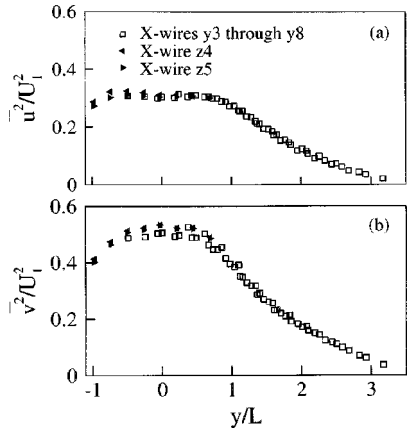

FIG. 2. Lateral distributions of (a) $\overline{u^2}/U_1^2$, (b) $\overline{v^2}/U_1^2$.

tional to velocity fluctuations u, v, and w, together with the local mean velocities $\overline{U}$, $\overline{V}(\approx 0)$ and $\overline{W}(\approx 0)$, were formed on digital tape. The duration of each record was about 38 s.

III. SOME PERFORMANCE CHECKS OF THE "VORTICITY PROBE"

Since vorticity was approximated using signals from four closely located X wires, it was important to ensure that the interference between these X wires was negligible. Distributions of $\overline{u^2}$ and $\overline{v^2}$ (Fig. 2) and u and v spectra (Fig. 3) obtained with X-wires z4 and z5 were nearly identical to those from y3 to y8, implying little interference between the two X wires. In addition, the $\overline{u^2}$ and $\overline{v^2}$ distributions from the two X wires of the "vorticity probe" collapse, implying good internal consistency of the measurements.

IV. APPROXIMATION OF VORTICITY COMPONENTS

The vorticity components are defined in terms of the derivatives of the instantaneous velocities $U=\overline{U}+u$, $V \approx v(\overline{V}\approx 0)$, and $W\approx w(\overline{W}\approx 0)$, where an overbar denotes time averaging. Since $\partial\overline{U}/\partial z$ is zero, large-scale approximations to the three components of vorticity at the center of X-wires y1, y2, z4, and z5 are

$$\omega_x=\frac{\partial W}{\partial y}-\frac{\partial V}{\partial z}=\frac{\partial w}{\partial y}-\frac{\partial v}{\partial z}\approx\frac{\Delta w}{\Delta y}-\frac{\Delta v}{\Delta z}, \tag{1a}$$

$$\omega_y=\frac{\partial U}{\partial z}-\frac{\partial W}{\partial x}=\frac{\partial u}{\partial z}-\frac{\partial w}{\partial x}=\frac{\Delta u}{\Delta z}-\frac{\Delta w}{\Delta x}, \tag{1b}$$

$$\omega_z=\frac{\partial V}{\partial x}-\frac{\partial U}{\partial y}=\frac{\partial v}{\partial x}-\frac{\partial(\overline{U}+u)}{\partial y}\approx\frac{\Delta v}{\Delta x}-\frac{\Delta(\overline{U}+u)}{\Delta y}. \tag{1c}$$

In computing vorticity, central finite differences between the two points on either side of the probe center, in both z and y directions, were used. In Eq. (1), $\Delta y(=3.45\,\text{mm})$ and Δz $(=4.9\,\text{mm})$ are the spacings between X-wires y1 and y2, z4 and z5, respectively; $\Delta x=-U_c(2\Delta t)$, where $\Delta t=1/f_{\text{sampling}}$ and $U_c=0.87U_\infty$ is the average convection velocity.[20] The value of Δx is approximately 3.40 mm close to Δy. The two derivatives with respect to x are given by

$$\frac{\Delta\nu}{\Delta x}=\frac{1}{U_c}\frac{\Delta\nu_0}{2\Delta t}=-\frac{1}{U_c}\frac{\nu_0(i+1)-\nu_0(i-1)}{2\Delta t}, \tag{2a}$$

$$\frac{\Delta w}{\Delta x}=-\frac{1}{U_c}\frac{\Delta w_0}{2\Delta t}=-\frac{1}{U_c}\frac{w_0(i+1)-w_0(i-1)}{2\Delta t}, \tag{2b}$$

where v_0 and w_0 are the means of the two ν values from X-wires z4 and z5, and the two w values from y1 and y2, respectively. For simplicity, the subscript "0" will be herein omitted. The central difference approximation was also used so that the six X wires, y3–y8, yielded the instantaneous vorticity at each of the five midway locations between adjacent X wires.[2]

V. ROOT MEAN SQUARE DISTRIBUTION AND SPECTRA

The rms values of ω_x, ω_y, and ω_z are shown in Fig. 4. Vorticity was first normalized by multiplying it with the factor L/U_1 [Fig. 4(a)]. The rms values of ω_z from the "vorticity probe" agree well with those from X-wires y3–y8, thus providing another internal consistency check of the data. The present measurement has been compared with that of Marasli *et al.*[17] and also Mi and Antonia.[21] Marasli *et al.* used a twelve sensor vorticity probe with a spatial resolution of about 2 mm, while Mi and Antonia used two X wires, which were separated by 1.2 mm. The latter authors applied corrections for the spatial resolution of their probe. Given the poor resolution of the present measurement, it is surprising that the present vorticity rms values are quite comparable with Marasli *et al.*'s values. Since these data were obtained at different Reynolds numbers, it is suspected that the Reynolds number effect is reflected in Fig. 4(a). Antonia *et al.*[12] noted that in self-preserving turbulent wall flows, enstrophy in the outer region scaled with $(U_\tau\delta/\nu)^{-1/2}(\delta/U_\tau)$, where U_τ is the friction velocity and δ is the boundary layer thickness or half-channel width. With U_τ and δ replaced by the maximum mean velocity deficit U_1 and the mean velocity half width L, respectively, this scaling was extended to free

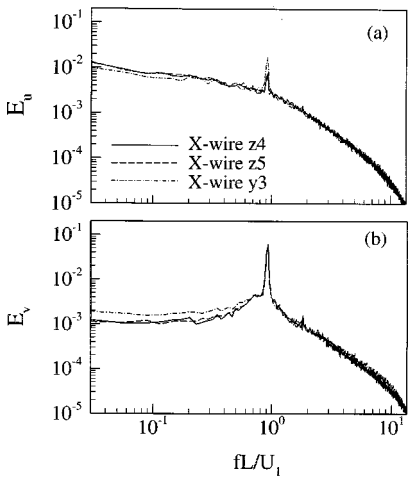

FIG. 3. Power spectral density functions of u and v $(y/L=0.5)$.

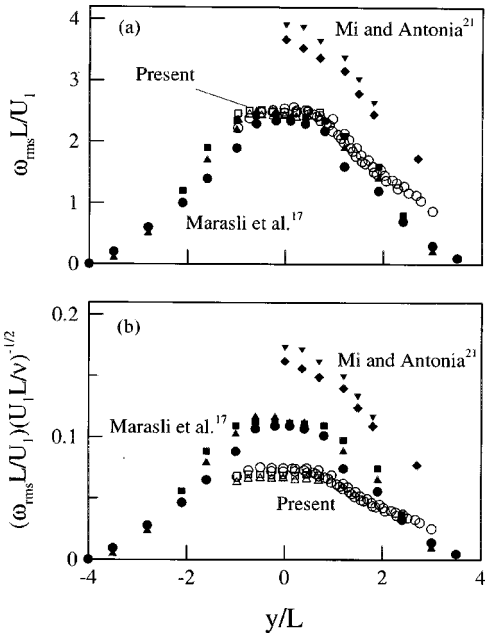

FIG. 4. Lateral distributions of $\omega_{x,\mathrm{rms}}$ (■, □), $\omega_{y,\mathrm{rms}}$ (▲, △, ▼), and $\omega_{z,\mathrm{rms}}$ (●, ○, ♦). □, △, ○: the present work; ■, ▲, ●: Marasli *et al.* (Ref. 17), Re=2000; ▼, ♦: Mi and Antonia (Ref. 21) Re=3000. (a) Normalized by L/U_1; (b) normalized by $(L/U_1)(U_1L/\nu)^{-1/2}$.

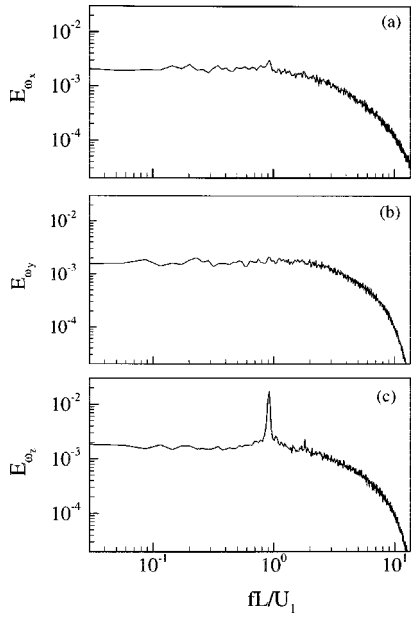

FIG. 5. Power spectral density functions of vorticity: (a) streamwise component ω_x, (b) lateral component ω_y, (c) spanwise component ω_z ($y/L=0.5$).

shear flows, such as jets and wakes. Sreenivasan[22] and also Zhou *et al.*[23] used this scaling for a plane wake. This scaling has subsequently been used since it accounts for the Reynolds number effect. The scaled vorticity magnitudes [Fig. 4(b)] are indeed smaller than those of Marasli *et al.* and Mi and Antonia, which is reconcilable with the poor spatial resolution of the present probe. Figure 4 indicates that the rms values of the three vorticity components are approximately the same.

Figure 5 presents the power spectral density functions E_{ω_x}, E_{ω_y}, and E_{ω_z} of ω_x, ω_y, and ω_z at nominally the same point. As expected, E_{ω_z} exhibits a strong peak at the shedding frequency $f_sL/U_1\approx0.93$, or $f_sd/U_\infty=0.20$, apparently as a result of the occurrence of pseudoperiodic spanwise vortices. A tiny peak is also identifiable in E_{ω_x} at $f_sL/U_1\approx0.93$, but not in E_{ω_y}. Marasli *et al.*[17] observed a peak at f_s in their ω_z spectrum in a circular cylinder wake at $x/d=30$ and Re=2000, but not in either ω_x or ω_y spectra. The present vorticity data were approximately deduced from velocity signals. At $x/d=20$, the ν fluctuation is strongly periodic. The major peak (at the shedding frequency) in the ν spectrum is far more pronounced than that in the u spectrum (Fig. 3). The w spectrum (not shown) does not exhibit a peak at the vortex shedding frequency. Further, the spacing Δz between X-wires z4 and z5 is quite large, about 4.9 mm. It seems therefore likely that the tiny peak in E_{ω_x} is caused by errors in calculating ω_x from the finitely spaced ν signals [see Eq. 1(a)].

The spectral coherence between f and g is defined as $\mathrm{Coh}_{f,g}=(\mathrm{Co}_{f,g}^2+Q_{f,g}^2)/E_fE_g$, where f and g each stand for either ω_x, ω_y, or ω_z, $\mathrm{Co}_{f,g}$ and $Q_{f,g}$ are the cospectrum and quadrature spectrum of f and g, respectively. $\mathrm{Coh}_{f,g}$ provides a measure of the degree of correlation between the Fourier components of f and g. $\mathrm{Coh}_{\omega_x,\omega_z}$ and $\mathrm{Coh}_{\omega_y,\omega_z}$ (Fig. 6) exhibit a peak at the shedding frequency. On the other hand, $\mathrm{Coh}_{\omega_x,\omega_y}$ does not indicate such a peak. The relatively strong coherence between ω_x and ω_z at the vortex shedding frequency suggests a close association between ribs and spanwise structures. Since the ribs are inclined in the (x, y) plane, the peak at f_s in $\mathrm{Coh}_{\omega_y,\omega_z}$ is not surprising. The phase angles $\Phi_{\omega_x,\omega_z}(\equiv Q_{\omega_x,\omega_z}/\mathrm{Co}_{\omega_x,\omega_z})$ and Φ_{ω_y,ω_z} (Fig. 7) corresponding to these peaks range between 0.5π and 0.7π. Here, the cross-spectrum is computed from the Fourier transform of the correlation $\overline{\omega_x(t+\tau)\omega_z(t)}$ or $\overline{\omega_y(t+\tau)\omega_z(t)}$. A positive

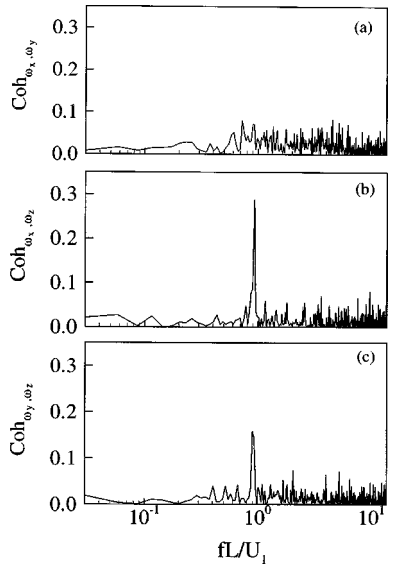

FIG. 6. Spectral coherence (a) $\mathrm{Coh}_{\omega_x,\omega_y}$ between ω_x and ω_y, (b) $\mathrm{Coh}_{\omega_x,\omega_z}$ between ω_x and ω_z, (c) $\mathrm{Coh}_{\omega_y,\omega_z}$ between ω_y and ω_z ($y/L=0.5$).

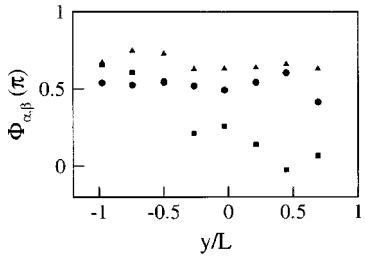

FIG. 7. Lateral distributions of spectral phase angles $\Phi_{\alpha,\beta}$ at the vortex shedding frequency: ■, $\alpha=\omega_x$, $\beta=\omega_y$; ▲, $\alpha=\omega_x$, $\beta=\omega_z$; ●, $\alpha=\omega_y$, $\beta=\omega_z$.

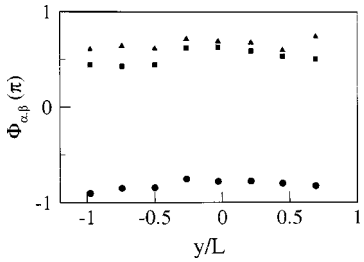

FIG. 9. Lateral distributions of spectral phase angles $\Phi_{\alpha,\beta}$ at the vortex shedding frequency: ■, $\alpha=uv$, $\beta=\omega_x$; ▲, $\alpha=uv$, $\beta=\omega_y$; ●, $\alpha=uv$, $\beta=\omega_z$.

phase means that ω_x or ω_y leads ω_z. Figure 7 shows that ω_x or ω_y leads ω_z at all lateral locations ($-1<y/L<0.7$). It seems that, provided ribs are responsible for the peaks in Fig. 6, they are not exactly midway between consecutive spanwise structures. This suggestion is supported by the conditional data in Sec. VII. The coherence between uv and ω_x signals and that between uv and ω_z (Fig. 8) also indicate a peak at the shedding frequency. The phase angle between uv and ω_z (Fig. 9) is about $-\pi$. This is reasonable since the Reynolds shear stress occurs primarily in the saddle region,[9] which is phase shifted by π relative to the dominating spanwise structures. The phase angle between uv and ω_x is between 0.5π and 0.6π, which is consistent with the value of Φ_{ω_x,ω_z}.

VI. INCLINATION OF THE VORTICITY VECTOR

The angles, defined by

$$\alpha=\tan^{-1}(\omega_y/\omega_x), \tag{3a}$$

$$\beta=\tan^{-1}(\omega_z/\omega_x), \tag{3b}$$

$$\gamma=\tan^{-1}(\omega_z/\omega_y), \tag{3c}$$

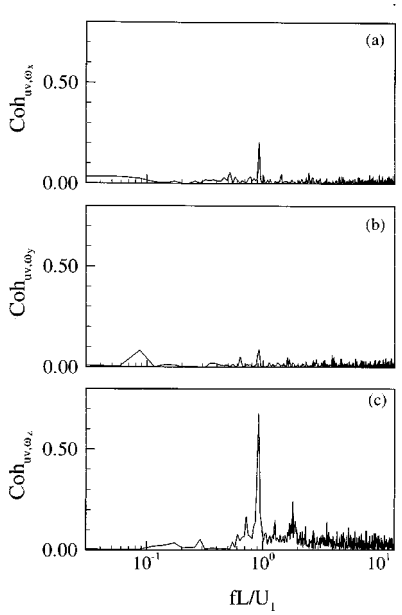

FIG. 8. Spectral coherence (a) $\mathrm{Coh}_{uv,\omega_x}$ between uv and ω_x, (b) $\mathrm{Coh}_{uv,\omega_y}$ between uv and ω_y, (c) $\mathrm{Coh}_{uv,\omega_z}$ between uv and ω_z ($y/L=0.5$).

provide some insight into the orientation of vortical structures.

Figure 10 shows the probability density function p of these angles for $y\geqslant 0$. Above the centerline, $p(\alpha)$ [Fig. 10(a)] has a significant peak at $\alpha\approx 50°$. As will be seen in Sec. VII, large values of ω_x and ω_y may occur both within spanwise structures as well as longitudinal structures. Arguably, the estimation of α would be arbitrary when the measurement point is within the spanwise structures. The peak is likely to be associated with the saddle region, as confirmed in Sec. VII. Although the peak is broad, it gives a reasonable indication of the most probable orientation of the ribs. The interpretation is consistent with Zhou and Antonia's finding[9] that ribs have an inclination of about 55° to the x axis and are approximately aligned with the diverging separatrix ($\approx 50°$) through the saddle. The slight difference ($\approx 5°$) between the results of Zhou and Antonia and the present ones can probably be ascribed to experimental uncertainty. Bisset *et al.*[11] found that $p(\alpha)$ peaked at $\alpha\approx 45°$ in the far wake. The same explanation may apply. The difference in α between the near and far wakes may not be entirely due to the experimental uncertainty. The spanwise vortical structures in the near wake have their origin in the vortex shedding process, while the dynamical process for the formation of the far-wake vortical structures is likely to be more complicated. One may surmise that vortical structures may exhibit different behaviors in near and far wakes.[24] The distribution of $p(\alpha)$ has another peak at about $-140°$, a shift of about 180° from the other peak. The near 180° period is probably a consequence of invariance with respect to the z axis. Both ω_x and ω_y change sign after reflection, i.e., the peak at $-140°$ is caused by the same phenomenon as that at 50°.[11,25] The distributions of $p(\beta)$ [Fig. 10(b)] and $p(\gamma)$ [Fig. 10(c)] are similar, although different from $p(\alpha)$. A broad peak occurs at $-90°$ and nothing is observed at 180°. Apparently, the predominantly negative spanwise vorticity associated with Karman vortices is orthogonal to ω_x and ω_y and cannot yield a value of $+90°$ for β or γ.

VII. CONDITIONAL DATA

A. Detection of spanwise vortical structures

Characteristic features of spanwise structures (e.g., a relatively sharp increase and decrease in u or v) were detected with the window average gradient (WAG) method de-

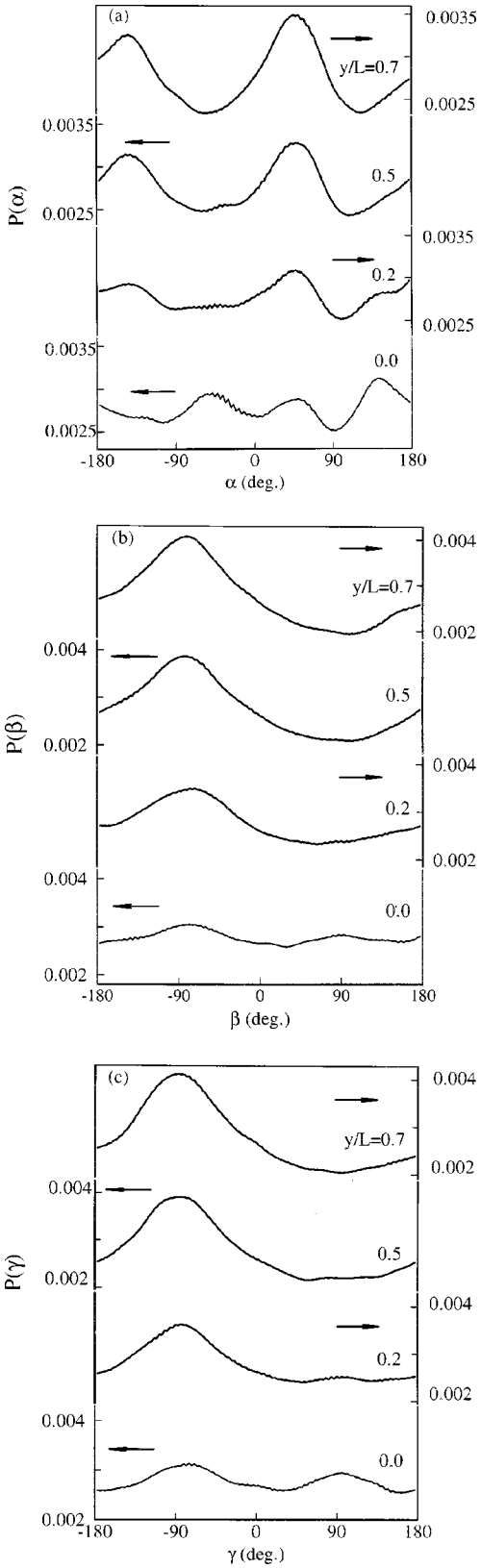

FIG. 10. Probability density functions of (a) $\alpha=\tan^{-1}(\omega_y/\omega_x)$, (b) $\beta=\tan^{-1}(\omega_z/\omega_x)$, (c) $\gamma=\tan^{-1}(\omega_z/\omega_y)$.

scribed in detail in Antonia and Fulachier[26] and Bisset *et al.*[11] Briefly, this scheme identifies a change (either an increase or decrease) in average signal level over a specified time interval. A computational window of length $2\sigma+1$

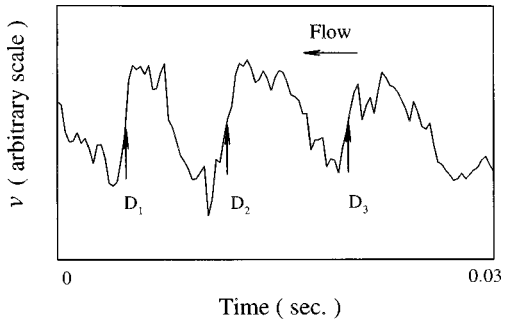

FIG. 11. Instantaneous trace of v at $y/L=0.5$. Detections using the WAG technique (D_1, D_2, and D_3 denote downstream detections) are shown.

points (digital samples) is moved point by point through the data, say $v(t_i)$ $(i=1,2,...,N,$ where N is the total number of data), and the value of WAG_j, where

$$\mathrm{WAG}_j=\frac{\mathrm{sign}}{2\sigma}\left(\sum_{i=j+1}^{j+\sigma} v(t_i)-\sum_{i=j-\sigma}^{j-1} v(t_i)\right),$$

$$j=\sigma+1,\sigma+2,...,N-\sigma. \tag{4}$$

The value of sign is $+1$ or -1, and σ is set equal to about half the number of data points corresponding to the average spanwise structure period.

A detection region begins when WAG_j first exceeds κv_{rms} where κ is a threshold chosen such that the average detection frequency is approximately equal to the average spanwise structure period; it ends when WAG_j drops below zero. The detection instant j_m within each detection region is the value of j for which WAG_j is largest. This occurs at the downstream and upstream regions when sign is $+1$ or -1, respectively.

The WAG technique was applied to $v(t_i)$. A total of about 2000 events were detected. Typical detections obtained for sign$=+1$ are shown in Fig. 11.

B. Conditional average

The conditional average of an instantaneous quantity F is given by

$$\langle F\rangle_k=\frac{1}{N}\sum_{m=1}^{N} F_{jm+k}, \tag{5}$$

where k represents time (in samples, positive or negative) relative to the detection points j_m. (For convenience, the subscript k will be omitted hereinafter.)

F can be viewed as the sum of the time mean component $\overline{F}$ and the fluctuation component f. The latter can be further decomposed into a coherent fluctuation $\tilde{f}\equiv\langle f\rangle$ and an incoherent fluctuation f', viz.

$$f=\tilde{f}+f'. \tag{6}$$

Also,

$$\langle fg\rangle=\tilde{f}\tilde{g}+\langle f'g'\rangle, \tag{7}$$

where f and g can each stand for either ω_x, ω_y, or ω_z.

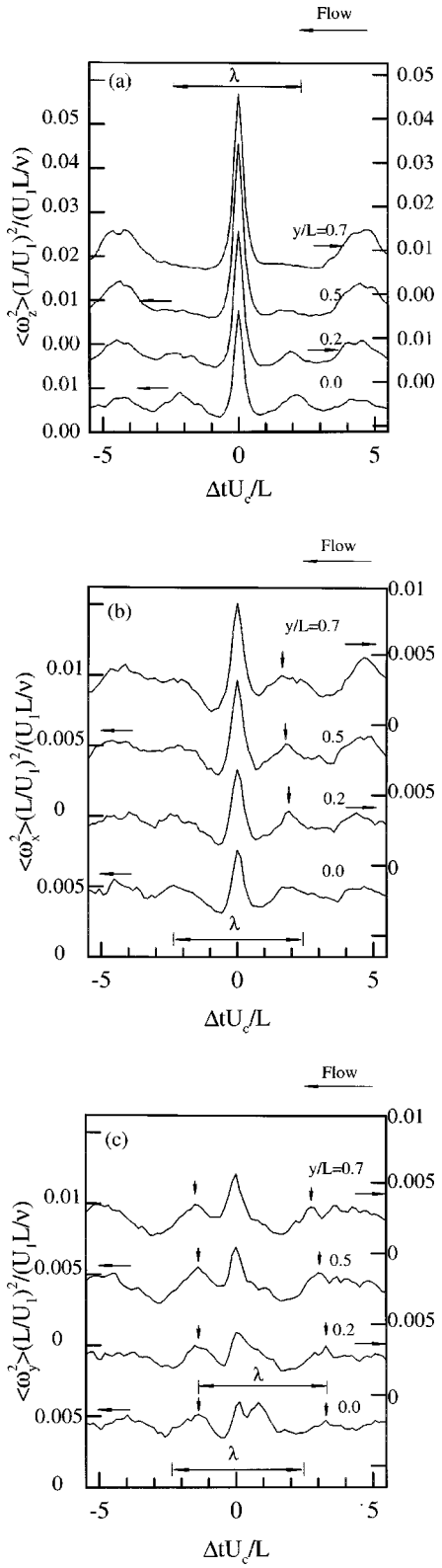

FIG. 12. Conditional averages based on WAG detections of the v signal (sign=1): (a) $\langle\omega_z^2\rangle(L/U_1)^2(U_1L/v)^{-1}$; (b) $\langle\omega_x^2\rangle(L/U_1)^2(U_1L/v)^{-1}$; (c) $\langle\omega_y^2\rangle(L/U_1)^2(U_1L/v)^{-1}$.

C. Conditional vorticity variance

Figure 12 presents the conditionally averaged vorticity variance on and above the centerline. There is a periodicity in all three components, with a value of λ, the average wavelength of the spanwise vortical structures, consistent with the Strouhal number. A strong peak or concentration occurs in $\langle\omega_z^2\rangle$ [Fig. 12(a)] at the detection instant ($\Delta tU_c/L=0$), indicating that detections are quite reasonable. The peak is strongest at $y/L=0.5$ and 0.7, apparently because the most probable location of the spanwise structure center is $y/L \approx y/d=0.5-0.9$.[9] Peaks can also be observed in $\langle\omega_x^2\rangle$ and $\langle\omega_y^2\rangle$ [Figs. 12(b) and 12(c)] near $\Delta tU_c/L=0$. Since turbulent vortical structures are highly three dimensional, it is not surprising that the relatively strong concentration of the streamwise and transverse vorticity components occurs near the peak of the spanwise component. This is not inconsistent with the observation in Fig. 7 that the phase angle at ($f=f_s$) between ω_z and ω_y or ω_z and ω_x lies between 0.5π and 0.7π. The quasiperiodical ω_z (at $f=f_s$) is expected to occur predominantly within spanwise structures. On the other hand, ω_y and ω_x may largely reside either within spanwise structures or in the saddle region, that is, ω_y and ω_x may have a phase angle, with respect to ω_z, of nearly zero or π. The combined effect could result in a phase angle of $0.5-0.7\pi$. The peak in $\langle\omega_y^2\rangle$ is less pronounced than that in $\langle\omega_x^2\rangle$; their corresponding magnitudes are about 20% and 30%, respectively, of the maximum of $\langle\omega_z^2\rangle$. The v signal has been used for detections. As a result, ω_x and ω_z, which are deduced from the v-containing signal [Eq. (1)], may tend to be emphasized whereas ω_y, which is not related to v, is not.

It is of interest to note that upstream of the detection, i.e., $\Delta tU_c/L=0$, of the spanwise structures, both $\langle\omega_x^2\rangle$ and $\langle\omega_y^2\rangle$ display peaks near the saddle point. Downstream of the detected spanwise structure, another peak between the saddle point and the detection instant is observed for $\langle\omega_y^2\rangle$ [Fig. 12(c)], but not so evident for $\langle\omega_x^2\rangle$ [Fig. 12(b)]. Occurring at a wavelength λ of about one spanwise structure from the upstream structure, this downstream peak is probably caused by the same types of structures. Therefore, only peaks upstream of the detection instant are discussed.

The occurrence of peaks in $\langle\omega_x^2\rangle$ and $\langle\omega_y^2\rangle$ near the saddle point is consistent with the presence of ribs.[4,8,9] When y/L decreases, the peaks shift upstream, as highlighted by the arrows in Fig. 12. This is consistent with the alignment of ribs with the diverging separatrix through the saddle point. However, the peak of $\langle\omega_x^2\rangle$ does not occur at the same $\Delta tU_c/L$ as $\langle\omega_y^2\rangle$. This can be explained via the orientation of vorticity vectors in the (x, y) plane. Figure 13 shows the probability density function $p(\alpha)$ at a fixed longitudinal location, relative to the detection instant. At $\Delta tU_c/L=0$ (detection instant), a mild peak in $p(\alpha)$ occurs at $\alpha=-25°$. At $\Delta tU_c/L=1.1, \alpha\approx-8°$, implying that $\langle\omega_y^2\rangle$ is small but $\langle\omega_x^2\rangle$ is large, as indicated by Figs. 12(b) and 12(c). When $\Delta tU_c/L$ is further increased, α approaches 60° at $\Delta tU_c/L=2.75$, so that $\langle\omega_y^2\rangle$ is large [Fig. 12(c)] but $\langle\omega_x^2\rangle$ is small [Fig. 12(b)]. These likely α values are insensitive to the lateral location; the variation is generally within 5° for $y/L \approx 0.2-0.7$. The fact that the rib orientation may vary significantly with $\Delta tU_c/L$ is consistent with the earlier observation [Fig. 10(a)] that $p(\alpha)$, based on all vorticity vectors, exhibits a broad peak. The likely rib orientation at different $\Delta tU_c/L$,

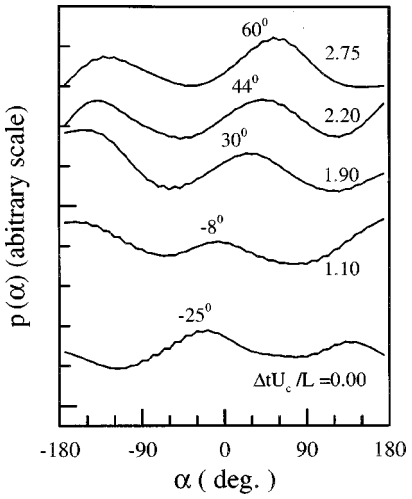

FIG. 13. Probability density function $p(\alpha)$ at different values of $\Delta tU_c/L$ $(y/L=0.7)$.

as exhibited in Fig. 13, further corroborates our argument that the peak in Fig. 10(a) is likely to be associated with the saddle region.

The variation in the likely α, with respect to $\Delta tU_c/L$, may, inter alia, be attributed to a significant variation in the lateral location y_c of spanwise structures[2,9] which escape detection by WAG. A possible scenario is sketched in Fig. 14. The rib wraps around a spanwise structure and is aligned along the diverging separatrix between consecutive spanwise structures. As y_c varies, the rib, when seen at a fixed lateral position, may change its orientation and streamwise location, relative to the spanwise structure or detection instant. At a relatively large y_c, the rib is ''seen'' further upstream, say at point *A*; the corresponding value of α is large, resulting in a large ω_y but small ω_x. On the other hand, at a smaller y_c, the rib appears closer, say at point *B*, to the spanwise structure so that α is smaller.

The variation in the lateral location y_c of spanwise structures has been well documented in the literature.[2,9] Over the last decade or so, many papers have dealt with the three dimensionality of the vortical structures, especially for smaller Reynolds numbers. Many aspects of this are now well understood. Flow visualizations[8,18] point to a waviness of the spanwise structures. This has been verified by direct numerical simulation (DNS) data.[27,28] The spanwise structures can be dislocated or shed in either parallel or oblique

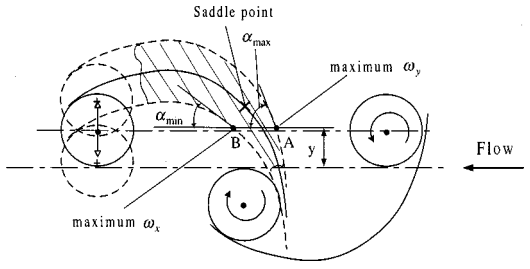

FIG. 14. Effect of the lateral variation of the vortex center on $\langle\omega_x^2\rangle$ and $\langle\omega_y^2\rangle$.

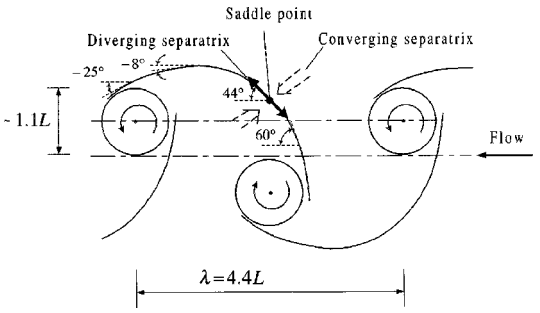

FIG. 15. Conceptual spatial relationship between spanwise structures and ribs.

modes.[18] All of these features may occur at larger Reynolds numbers and contribute to a variation in y_c.

Flow visualization and DNS data[8,18,29,30] at smaller Reynolds numbers have indicated that the rib connects consecutive counter-rotating spanwise structures on either side of the centerline. This may also apply at larger Reynolds numbers, as suggested by the fact that beyond the midpoint $(\Delta tU_c/L\approx 2.2)$, the most probable α (Fig. 13) at a fixed longitudinal location increases with $\Delta tU_c/L$. If, instead, the rib connects consecutive spanwise structures of the same sign, as is the case in a mixing layer,[31,32] the most probable α at a fixed longitudinal location should decrease as $\Delta tU_c/L$ increases.

Previous work[27,28,33,34] at small Reynolds numbers has suggested that there are two modes of streamwise structures. Mode *A* is of relatively large scale with a spanwise wavelength of about $4d$. Mode *B* has a significantly finer scale and a spanwise wavelength of $1d$. If these two modes also occur at higher Reynolds numbers, the streamwise structure, as represented in Fig. 14, is more likely to be a manifestation of mode *A*, rather than mode *B*, since the spatial resolution of the present measurements is inadequate for capturing mode *B* structures.

On the basis of the present data and previous observations, a schematic representation of the spatial relationship between spanwise structures and ribs is proposed and constructed in Fig. 15. For simplicity, the spanwise rolls are drawn as two-dimensional structures with a circular cross section. The actual spanwise structures should be elliptical, with the major axis approximately in the lateral direction.[9]

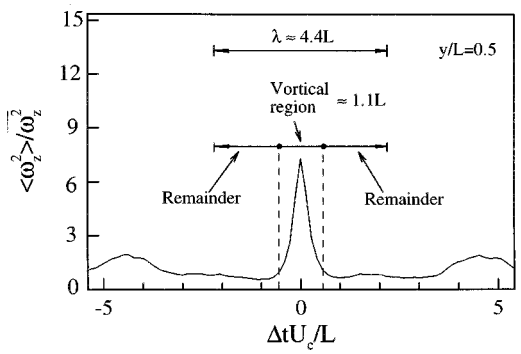

FIG. 16. Conditional average $\langle\omega_z^2\rangle/\overline{\omega_z^2}$ based on WAG detections of the v signal (sign$=+1$), $y/L=0.5$.

The likely orientation (Fig. 13) of ribs at different longitudinal locations is indicated in Fig. 15. At the midpoint (the saddle point) between consecutive spanwise structures, the rib is aligned along the diverging separatrix, at approximately 44° to the x axis. Note that this angle should not be confused with the most likely orientation (50°) of ribs [Fig. 10(a)], which is obtained based on the vorticity vectors of all longitudinal locations. The rib connects cross-stream spanwise structures of opposite sign.[18] The picture depicted in Fig. 15 also seems consistent with available flow visualizations and numerical data, e.g., Refs. 8, 18, 28–30, 33, and 35.

D. Structural average

With the conditionally averaged structure beginning k_1 samples before the detection instant and ending k_2 samples after this instant, a structural average, denoted by a double overbar, may be defined as follows:

$$\langle \overline{\overline{fg}} \rangle = \frac{1}{k_1+k_2+1} \sum_{-k_1}^{k_2} \langle fg \rangle. \tag{8}$$

The value of $k_1(=k_2)$ is 16 so that the duration (k_1+k_2+1) corresponds approximately to the average period of the spanwise structures. The ratio of $\overline{\overline{fg}}$ or $\overline{\overline{f'g'}}$ to $\overline{fg}$ provides a useful measure of the coherent and incoherent contributions to $\overline{fg}$. Since the coherent contribution is based on detections of spanwise vortical structures, the contribution from ribs to the streamwise vorticity component may not be taken into account.

The flow may be divided into the vortical region and the ''remainder.'' The vortical region is identified with the strong concentration of the large-scale spanwise vorticity and the ''remainder'' is associated with the weak concentration, as illustrated in Fig. 16. The streamwise extent of the thus defined vortical region varies with the lateral location, ranging from about 1.0 to 1.3 L or 1.0 to 1.3d [Fig. 12(a)], i.e., about 23%–30% of the total space. The vortical region is conceptually consistent with the vortex size defined in terms of a minimum conditional vorticity level by Hussain and Hayakawa[1] and Zhou and Antonia.[2] The latter authors estimated the vortex size to be of the order of one cylinder diameter. Contributions to vorticity from the vortical region of the flow and the ''remainder'' may be estimated by weighting structural averages in proportion to the longitudinal extent λ of each region, namely

$$\langle \overline{\overline{fg}} \rangle_v^* = [\lambda_v/\lambda] \langle \overline{\overline{fg}} \rangle_v, \tag{9a}$$

$$\langle \overline{\overline{fg}} \rangle_r^* = [\lambda_r/\lambda] \langle \overline{\overline{fg}} \rangle_r, \tag{9b}$$

where the asterisk denotes the contribution to vorticity from either region and the subscripts v and r refer to the vortical region and the ''remainder,'' respectively.

The value of $\langle \overline{\overline{fg}} \rangle_{\text{sum}}^* = \langle \overline{\overline{fg}} \rangle_v^* + \langle \overline{\overline{fg}} \rangle_r^*$ (Figs. 17–19) is to within 10% of that for $\overline{fg}$. This suggests that, at least for vorticity, the combination of the selected vortical regions and the ''remainder'' is representative of the flow. The variances of the streamwise and transverse vorticity components do not vary significantly with y, although the variance of the spanwise component does. The ''remainder'' contributes more to $\overline{\omega_x^2}$ and $\overline{\omega_y^2}$ than the vortical region; $\langle \overline{\overline{\omega_x^2}} \rangle_r^* / \overline{\omega_x^2}$ and $\langle \overline{\overline{\omega_y^2}} \rangle_r^* / \overline{\omega_y^2}$ [Figs. 17(a) and 17(b)] are equal to about 60%. On the other hand, the vortical region contributes about 40%. Note that coherent contribution to $\overline{\omega_x^2}$ and $\overline{\omega_y^2}$ [Figs. 18(a) and 18(b)] is very small, less than 1%. Longitudinal structures may have vorticities of opposite sign. Positive and negative vorticities may cancel each other during the conditional averaging based on detections of spanwise vortical structures, resulting in a negligibly small $\overline{\langle \overline{\omega_x} \rangle^2}^* / \overline{\omega_x^2}$ and $\overline{\langle \overline{\omega_y} \rangle^2}^* / \overline{\omega_y^2}$. For the spanwise component, the vortical region dominates, the ratio $\langle \overline{\overline{\omega_z^2}} \rangle_v^* / \overline{\omega_z^2}$ [Fig. 17(c)] being between 60% and 80%. The coherent contribution [Fig. 18(c)] is almost entirely from the vortical region. But the ''remainder'' accounts for most of the incoherent vorticity [Fig. 19(c)].

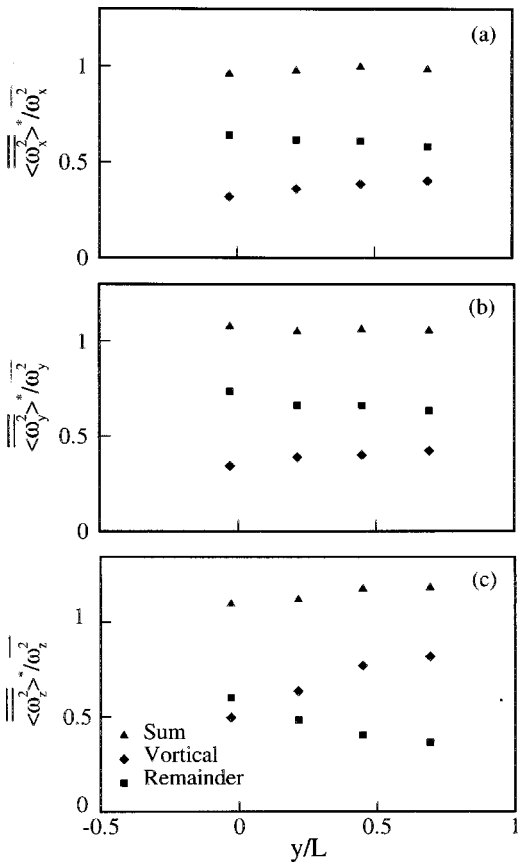

FIG. 17. Lateral distributions of (a) $\langle \overline{\overline{\omega_x^2}} \rangle^* / \overline{\omega_x^2}$, (b) $\langle \overline{\overline{\omega_y^2}} \rangle^* / \overline{\omega_y^2}$, (c) $\langle \overline{\overline{\omega_z^2}} \rangle^* / \overline{\omega_z^2}$ for the vortical region (◆), the ''remainder'' (■), and their sum (▲).

VIII. CONCLUSIONS

Longitudinal and spanwise structures in a turbulent near wake $(x/d=20)$ have been investigated using simultaneously obtained (large-scale) approximations to the three vorticity components. The present measurements provide useful qualitative information on the likely interrelationships between the two types of vortical structures. Conditional distributions of $\langle \omega_x^2 \rangle$ and $\langle \omega_y^2 \rangle$ exhibit maxima near the location where the spanwise structure is detected. These maxima are

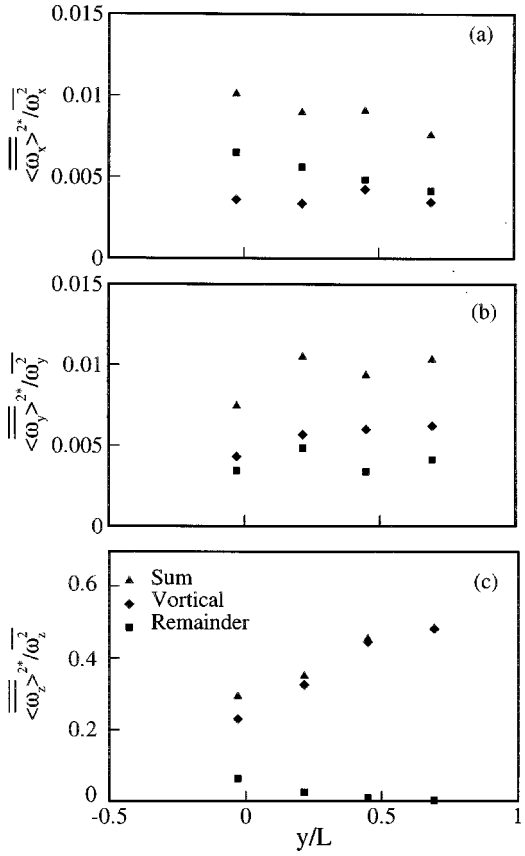

FIG. 18. Lateral distributions of (a) $\overline{\langle\omega_x\rangle^{2*}}/\overline{\omega_x^2}$, (b) $\overline{\langle\omega_y\rangle^{2*}}/\overline{\omega_y^2}$, (c) $\overline{\langle\omega_z\rangle^{2*}}/\overline{\omega_z^2}$ for the vortical region (♦), the ''remainder'' (■), and their sum (▲).

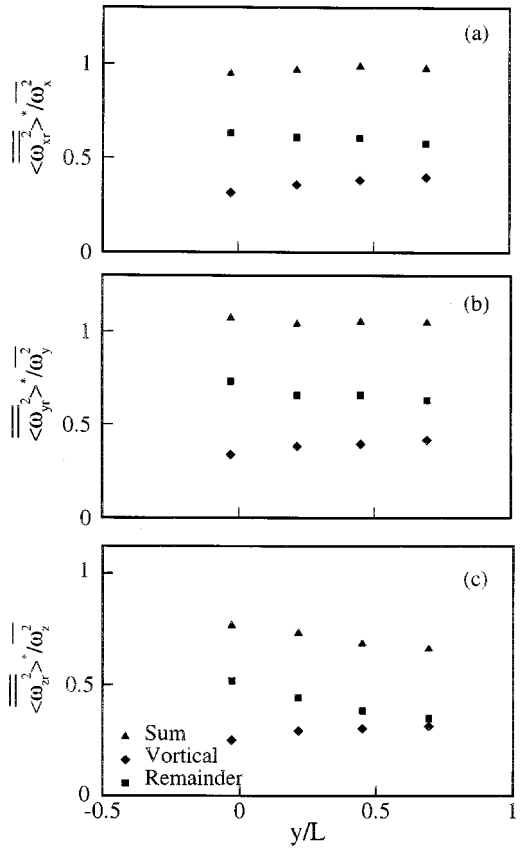

FIG. 19. Lateral distributions of (a) $\overline{\langle\omega_{xr}^2\rangle^*}/\overline{\omega_x^2}$, (b) $\overline{\langle\omega_{yr}^2\rangle^*}/\overline{\omega_y^2}$, (c) $\overline{\langle\omega_{zr}^2\rangle^*}/\overline{\omega_z^2}$, for the vortical region (♦), the ''remainder'' (■), and their sum (▲).

attributed to the three dimensionality of the spanwise structures. There is a peak in $\langle\omega_x^2\rangle$ near the saddle point between spanwise structures, whereas $\langle\omega_y^2\rangle$ displays a maximum between the saddle point and the detection point of the spanwise structures. These concentrations of $\langle\omega_x^2\rangle$ and $\langle\omega_y^2\rangle$, together with the probability density function of the angle of vorticity vectors projected in the (x, y) plane, point to the presence of ribs. Based on the present data and previous observations, a schematic spatial relationship is proposed and constructed. It appears that ribs are closely associated with the spanwise vortices. In this model, the ribs, oriented with the diverging separatrix through the saddle point, connect consecutive spanwise structures on either side of the centerline. Despite the significant scatter, the most probable rib orientation is about 50° to the x axis. This model is consistent with previous flow visualizations and DNS data at relatively low Reynolds numbers (Refs. 8, 18, 28–30, 33, and 35).

About 40% of either $\overline{\omega_x^2}$ or $\overline{\omega_y^2}$ is associated with spanwise vortical structures, apparently resulting from the three dimensionality of these structures. The remaining 60% may be largely attributed to ribs. The coherent contribution to $\overline{\omega_x^2}$ and $\overline{\omega_y^2}$, based on WAG detections, is negligible, probably due to the cancellation of opposite-signed vorticities. About 60%–80% of $\overline{\omega_z^2}$ occurs within spanwise vortical structures. The coherent contribution to $\overline{\omega_z^2}$ comes almost entirely from the vortical region, whereas the incoherent contribution is mainly from the ''remainder.''

ACKNOWLEDGMENTS

Y.Z. wishes to acknowledge financial support from the Research Grants Council of the Government of the HKSAR through Grant No. PolyU5161/97E. R.A.A. is grateful for the continuing support of the Australian Research Council. Dr. J. Mi's contribution to the experimental work is greatly appreciated.

[1] A. K. M. F. Hussain and M. Hayakawa, ''Eduction of large-scale organized structures in a turbulent plane wake,'' J. Fluid Mech. **180**, 193 (1987).
[2] Y. Zhou and R. A. Antonia, ''A study of turbulent vortices in the near wake of a cylinder,'' J. Fluid Mech. **253**, 643 (1993).
[3] M. Kiya and M. Matsumura, ''Incoherent turbulence structure in the near wake of a normal plate,'' J. Fluid Mech. **190**, 343 (1988).
[4] M. Hayakawa and F. Hussain, ''Three-dimensionality of organized structures in a plane turbulent wake,'' J. Fluid Mech. **206**, 375 (1989).
[5] E. Meiburg and J. C. Lasheras, ''Experimental and numerical investigation of the three-dimensional transition in plane wakes,'' J. Fluid Mech. **190**, 1 (1988).
[6] C. H. K. Williamson, ''The existence of two stages in the transition to three-dimensionality of a cylinder wake,'' Phys. Fluids **31**, 3165 (1988).
[7] B. Bays-Muchmore and A. Ahmed, ''On streamwise vortices in turbulent wakes of cylinders,'' Phys. Fluids A **5**, 387 (1993).
[8] J. Wu, J. Sheridan, M. C. Welsh, and K. Hourigan, ''Three-dimensional vortex structures in a cylinder wake,'' J. Fluid Mech. **312**, 201 (1996).

[9]Y. Zhou and R. A. Antonia, ''Critical points in a turbulent near-wake,'' J. Fluid Mech. **275**, 59 (1994).
[10]R. A. Antonia, T. Zhou, and Y. Zhu, ''Three-component vorticity measurements in a turbulent grid flow,'' J. Fluid Mech. **374**, 29 (1998).
[11]D. K. Bisset, R. A. Antonia, and D. Britz, ''Structure of large-scale vorticity in a turbulent far wake,'' J. Fluid Mech. **218**, 463 (1990).
[12]R. A. Antonia, S. Rajagopalan, and Y. Zhu, ''Scaling of mean square vorticity in turbulent flows,'' Exp. Fluids **20**, 393 (1996).
[13]J.-L. Balint, J. M. Wallace, and P. Vukoslavcevic, ''The statistical properties of the vorticity field of a two-stream turbulent mixing layer,'' *Advances in Turbulence*, edited by H. H. Fernholz and H. E. Fiedler (Springer, New York, 1989), Vol. II, pp. 74–78.
[14]J.-L. Balint, J. M. Wallace, and P. Vukoslavcevic, ''The velocity and vorticity vector fields of a turbulent boundary layer. 2. Statistical properties,'' J. Fluid Mech. **228**, 53 (1991).
[15]A. Tsinober, E. Kit, and T. Dracos, ''Experimental investigation of the field of velocity gradients in turbulent flows,'' J. Fluid Mech. **242**, 169 (1992).
[16]G. C. Lemonis, ''An experimental study of the vector fields of velocity and vorticity in turbulent flows,'' Ph.D. thesis, Swiss Federal Institute of Technology, Zurich, 1995.
[17]B. Marasli, P. Nguyen, and J. M. Wallace, ''A calibration technique for multiple-sensor hot-wire probes and its application to vorticity measurements in the wake of a circular cylinder,'' Exp. Fluids **15**, 209 (1993).
[18]C. H. K. Williamson, ''Vortex dynamics in the cylinder wake,'' Annu. Rev. Fluid Mech. **28**, 477 (1996).
[19]A. Prasad and C. H. K. Williamson, ''Three-dimensional effects in turbulent bluff-body wakes,'' J. Fluid Mech. **343**, 235 (1997).
[20]Y. Zhou and R. A. Antonia, ''Convection velocity measurements in a cylinder wake,'' Exp. Fluids **13**, 63 (1992).
[21]J. Mi and R. A. Antonia, ''Vorticity characteristics of the turbulent intermediate wake,'' Exp. Fluids **20**, 383 (1996).
[22]K. R. Sreenivasan, ''The energy dissipation in turbulent shear flows,'' in *Symposium on Developments in Fluid Dynamics and Aerospace Engineering*, edited by S. M. Deshpande, A. Prabhu, K. R. Sreenivasan, and P. R. Viswanath, Bangalore (Interline, 1995), p. 159.
[23]Y. Zhou, W. K. Tsang, and R. A. Antonia, ''Vortical structures in a turbulent far-wake: Effect of Reynolds number,'' Fluid Dyn. Res. **25**, 293 (1999).
[24]Y. Zhou and R. A. Antonia, ''Memory effects in a turbulent plane wake,'' Exp. Fluids **19**, 112 (1995).
[25]P. Moin and J. Kim, ''The structure of the vorticity field in turbulent channel flow. 1. Analysis of instantaneous fields and statistical correlations,'' J. Fluid Mech. **155**, 441 (1985).
[26]R. A. Antonia and L. Fulachier, ''Topology of a turbulent boundary with and without wall suction,'' J. Fluid Mech. **198**, 429 (1989).
[27]M. Thompson, K. Hourigan, and J. Sheridan, ''Three-dimensional instabilities in the cylinder wake,'' International Colloquium on Jets, Wakes, Shear Layers, Melbourne, Australia 18–20 April 1994 (unpublished), paper 10.
[28]H.-Q. Zhang, U. Fey, B. R. Noack, M. König, and H. Eckelmann, ''On the transition of the cylinder wake,'' Phys. Fluids **7**, 779 (1995).
[29]M. Brede, H. Eckelmann, and D. Rockwell, ''On secondary vortices in the cylinder wake,'' Phys. Fluids **8**, 2117 (1996).
[30]J.-C. Lin, P. Vorobieff, and D. Rockwell, ''Space-time imaging of a turbulent near-wake by high-image-density particle image cinematography,'' Phys. Fluids **8**, 555 (1996).
[31]L. P. Bernal and A. Roshko, ''Streamwise vortex structure in plane mixing layers,'' J. Fluid Mech. **170**, 499 (1986).
[32]J. C. Lasheras and H. Choi, ''Three-dimensional instability of a plane free shear layer: An experimental study of the formation and evolution of streamwise vortices,'' J. Fluid Mech. **189**, 53 (1986).
[33]R. D. Henderson, ''Nonlinear dynamics and pattern formation in turbulent wake transition,'' J. Fluid Mech. **352**, 65 (1997).
[34]H. Mansy, P. Yang, and D. R. Williams, ''Quantitative measurements of three-dimensional structures in the wake of a circular cylinder,'' J. Fluid Mech. **270**, 277 (1994).
[35]R. Elavarasan, L. Djenidi, and R. A. Antonia, ''A study of the near-wake region of a circular cylinder,'' Ninth International Symposium on Applications of Laser Techniques to Fluid Mechanics, Lisbon, 1998 (unpublished), Vol. I, pp. 2.1.1–2.1.5.